ISPRS Journal of Photogrammetry and Remote Sensing 64 (2009) 551–560

Contents lists available at ScienceDirect

ISPRS Journal of Photogrammetry and Remote Sensing

journal homepage: www.elsevier.com/locate/isprsjprs

Co-registration and correlation of aerial photographs for ground deformation measurements

François Ayoub*, Sébastien Leprince, Jean-Philippe Avouac

California Institute of Technology, 1200 East California Blvd, Pasadena, CA 91125, USA

ARTICLE INFO

Article history:
Received 26 January 2007
Received in revised form
24 March 2009
Accepted 26 March 2009
Available online 2 May 2009

Keywords:
Aerial
Photography
Change detection
Registration
Correlation

ABSTRACT

We describe and test a procedure to accurately co-register and correlate multi-temporal aerial images. We show that this procedure can be used to measure surface deformation, and explore the performance and limitations of the technique. The algorithms were implemented in a software package, COSI-Corr (available from the Caltech Tectonics Observatory website). The technique is validated on several case examples of co-seismic deformation. First, we measure co-seismic ground deformation due to the 1992, Mw 7.3, Landers, California, earthquake from 1 m resolution aerial photography of the National Aerial Photography Program (United States Geological Survey). The fault ruptures are clearly detected, including small kilometric segments with fault slip as small as a few tens of centimeters. We also obtained similar performance from images of the fault ruptures produced by the 1999 Mw 7.1 Hector Mine, California, earthquake. The measurements are shown to be biased due to the inaccuracy of the Digital Elevation Model, film distortions, scanning artifacts, and ignorance of ground displacements at the location of the tie points used to co-register the multi-temporal images. We show that some of these artifacts can be identified and corrected.

1. Introduction

In principle, ground displacements can be tracked through cross-correlation or feature tracking on multitemporal aerial photographs. This approach has been used with some success for a variety of applications, e.g., landslides (Delacourt et al., 2004), volcano (de Michele and Briole, 2007), and is of particular interest in seismotectonics. Large earthquakes generally produce ground ruptures which are an important source of information on earthquake mechanics in complement to geodetic and seismological measurements. Field measurements suffer from a number of limitations: fault ruptures have a complex geometry and the zone of anelastic co-seismic strain is sometimes distributed and difficult to detect in the field; fault slip can generally be measured only on a limited number of locations where clear offset piercing points are observable such as roads or terrace risers for example; the fault-perpendicular component is generally not measurable in the field. Optical satellite imagery can help overcome some of these limitations, the principle of the approach being that surface deformation can be measured by co-registration and correlation of images acquired before and after an earthquake (Van Puymbroeck et al., 2000). The technique has been implemented for operational use in a software for Co-Registration of Optically Sensed Images and Correlation (COSI-Corr) (Leprince et al., 2007), available from the Caltech Tectonics Observatory (http://www.tectonics.caltech.edu). The technique has proven effective in a number of studies of large, Mw $>$ 7, earthquakes (Avouac et al., 2006; Binet and Bollinger, 2005; Dominguez et al., 2003; Feigl et al., 2002; Klinger et al., 2005; Michel and Avouac, 2002). However, the resolution of satellite images, e.g., 2.5–10 m SPOT, 15 m ASTER, is sometimes insufficient to measure subtle fault displacement less than about 1 m (Leprince et al., 2007) and is therefore of limited use to analyze the details of co-seismic deformation or to investigate earthquakes with magnitude Mw less than 7. In addition, satellite images with appropriate geometric accuracy and ground resolution are not available for some past earthquakes which are known to have produced surface ruptures. The use of aerial photography with sub-metric ground resolution would extend the applicability of the technique to earthquakes too small to be measured from satellite images, or for which good quality satellite images would not be available. Michel and Avouac (2006) obtained encouraging results on the 1992 Landers earthquake using aerial photography from the United States Geological Survey (USGS). Motivated by this result, we have adapted to aerial images the procedure designed by Leprince et al. (2007) for the processing of satellite images. Hereafter, we describe this adaptation and assess the performance and limitations of the technique.

* Corresponding address: Caltech, M/C 100-23, 1200 East California Blvd, Pasadena, CA 91125, USA. Tel.: +1 626 395 3726; fax: +1 626 395 1740.
E-mail address: fayoub@gps.caltech.edu (F. Ayoub).
URL: http://www.tectonics.caltech.edu/slip_history/spot_coseis/ (F. Ayoub).

0924-2716/$ – see front matter
doi:10.1016/j.isprsjprs.2009.03.005

Retrieving accurate ground deformation of sub-resolution amplitude requires a number of processing steps. Prior to comparison, images must be finely co-registered. This is achieved by orthorectifying the images on a common projection while accounting for acquisition distortion, scaling difference, and topography. Special attention needs to be paid to the resampling to preserve the original image information. Ultimately, the correlation of the reconstructed images provides a map of the horizontal ground displacements.

We first detail the various steps in the processing: reconstruction mapping; resampling; co-registration optimization, and correlation. We next show an application to the 1992, Mw 7.3, Landers, California, earthquake. The technique is validated and sources of artifacts due to the scanning quality and to topographic distortions are identified and investigated. Finally, we present an application to the 1999, Mw 7.1, Hector Mine, California, earthquake to illustrate that, in the case of co-seismic deformation measurements, some ambiguity between real ground displacement and mis-registration can arise, and we show how this ambiguity can be resolved.

2. Methodology

2.1. Technique overview

The technique requires the digitization of the film based photographs with a high spatial and radiometric resolution scanner. Digital photography is not considered in this study as aerial photography archives are mainly film based. However, the technique described in this paper could be used with digital frame cameras as well.

Prior to comparison, images are co-registered through their orthorectification on a common reference system. Cumulative uncertainties on both the acquisition parameters and topography lead to mis-registrations between the orthorectified images to be compared. The co-registration is therefore improved by optimizing the acquisition parameters of the second image (the slave) with respect to the first orthorectified image (the master).

Orthorectified and precisely co-registered images are then correlated using a sliding window. At each step, horizontal offsets along the East/West and North/South directions are measured and stored.

2.2. Orthorectification & resampling

We chose to orthorectify the images on the UTM grid for the following reasons: it provides a support independent from the acquisition system, allowing the pairing of images from different devices, e.g., satellite and aerial images; the relative displacements between orthorectified images are directly measured in length unit; the orthorectified images are cartographically correct, possibly a useful by-product.

The orthorectification transformation is defined using photogrammetry technique (Wolf and Dewitt, 2000); that is, definition of the camera's Interior Orientation (IO), and Exterior Orientation (EO) with the help of Ground Control Points (GCPs). The orthorectification transform, which associates ground coordinates (UTM in our case) to pixel coordinates, is applied to the UTM grid on which the images are projected. This defines the transformation matrices, containing the x and y coordinates of the pixels in the image to project.

The orthorectified images are constructed by resampling the raw images according to the transformation matrices. It is common practice to use the nearest neighbor, bilinear, or bicubic kernel for resampling. However, these kernels can corrupt the image information by introducing aliasing and may ultimately bias the correlation (Leprince et al., 2007). We therefore use the ideal sine cardinal (*sinc*) kernel, truncated to a length between 11 and 25 samples, and whose lobes are determined from the transformation matrices.

2.3. GCP selection

GCPs are used to define an image's EO. A common method in selecting GCPs consists in measuring in-situ ground coordinates of features clearly identifiable on the image. This method is costly and might not be applicable depending on the area accessibility. The need for GCPs can be alleviated if on-board Kinematic GPS (KGPS) and Inertial Navigation Unit (INU) estimate directly the image's EO (Schwarz et al., 1993). The use of KGPS and INU have been common practice for the last couple of years. However, for more generality and to include older (pre-KGPS/INU) photographs, our approach assumes that the EO is not constrained from these techniques, and that no field measurements of GCPs are available.

GCPs are selected on the master image to obtain a proper orthorectified master with a minimum of topographic distortion. This requires georeferencing the image to the DEM as precisely as possible. Based on feature recognition, tie points are selected between the raw master and some external data such as a high resolution map, or an already georeferenced image (SPOT, aerial image, etc). The georeferencing of the external data (map, …) provides the horizontal coordinates, while the elevation is read from the DEM. If no external data are available, the shaded DEM can be used to define GCPs. In this case, the DEM provides both horizontal and vertical coordinates. Although this method works well with medium/high resolution satellites, it suffers from large inaccuracies with aerial images due to the usually large difference in resolution with the DEM. GCPs optimization explained in 2.4 allows some refinement generally yielding good results.

Once the master image is orthorectified, GCPs are selected on the slave image to achieve the best co-registration with the orthorectified master image. The slave's GCPs are defined by selecting tie points between the orthorectified master and the raw slave. The georeferenced master provides the horizontal ground coordinates while the DEM provides the elevation.

For our application of co-seismic ground deformation measurement, it might not be possible to define GCPs outside the deformation zone. Indeed, the footprint of aerial photographs is typically on the order of a few kilometers, while the deforming zone of earthquakes large enough to produce ground ruptures (with magnitudes Mw $>$ 6.5) is generally several tens of kilometers wide. As a consequence, selecting tie points between images bracketing the seismic event may introduce systematic error, since the ground coordinates of the slave tie points may have changed. In that case, information on ground deformation at the scale of the area covered by the GCPs is filtered out but the deformation at much smaller wavelengths such as the fault trace, the fault slip, and the near-field deformation, will still be retrieved. Satellite images with a larger footprint like SPOT (60 $\times$ 60 km) generally contain areas far enough from the main deformation (i.e., away from the fault trace) where GCPs can be selected without introducing significant errors. If, for example, external data on ground deformation are available through, e.g., field survey, GPS measures, or SPOT correlation maps, it is then possible to correct for GCPs' ground coordinates that have undergone co-seismic displacement. Tie points are selected as previously explained, and ground coordinates retrieved from the orthorectified master are corrected according to these external data. Alternatively, the theoretical displacements at the GCPs locations can be estimated from an a priori earthquake source model (Hudnut et al., 1994).

2.4. Co-registration optimization

Manual tie points selection leads to unavoidable mis-registrations between the orthorectified master and the orthorectified slave. However, these mis-registrations can be reduced afterwards by optimizing the slave GCPs as follows:

(1) Start with the GCPs derived from the tie points selected between the orthorectified master and the slave image.
(2) Estimate of the slave's EO based on the GCPs.
(3) Orthorectification of the slave image and correlation with the orthorectified master image.
(4) Correction of each GCP ground coordinate based on the ground offset found between the master and slave orthorectified images at each GCP location.
(5) Return to (2) with the updated GCPs ground coordinates. Iterate until ground offset found between the master and slave images become negligible.

In practice, to reduce computation time, only patches centered around each GCP are orthorectified and correlated.

The optimized GCPs generally lead to a sub-pixel co-registration between the orthorectified images. This optimization suppresses the need for a meticulous and time consuming precise tie point selection; a manual, coarse selection is sufficient as the optimization adjusts GCP coordinates. Nevertheless, tie points must be selected in areas where correlation has a good chance of succeeding (good local texture), and where no obvious temporal change may bias the correlation (e.g., strong shadow, man made changes). Residual mis-registration comes from all the artifacts (e.g., DEM error, acquisition distortions) which were left unaccounted for.

GCP optimization can also be applied to the master if its GCPs were to be determined from an already orthorectified image. The shaded DEM can be used as the master image, but this method is more subject to decorrelations, and correlation is generally possible only in areas with rough, vegetation-free topography.

It should be noted that the procedure assumes the topography unchanged between acquisitions, so that the slave and master images can be orthorectified using the same DEM. This is only an approximation. Theoretically, one should instead use a pre- and post- earthquake DEM to orthorectify the pre- and post-earthquake images, respectively, to account for the change in topography. Unfortunately, access to a pre- and post-earthquake DEM is rare. Also, given the uncertainties of the DEM values and georeferencing, which are generally large compared to the aerial photography resolution, it is best to use a single DEM: the orthorectification errors due to the DEM errors might be presumed to affect similarly the orthorectification of the master and slave images. We will see later that this approximation is a source of systematic error that can be corrected.

2.5. Correlation

To measure precisely the relative offset between two images, several methods have been proposed in the literature. The one used in this study is based on phase correlation and described in detail in Leprince et al. (2007). The correlation method must be robust to noise and sub-pixel accurate, while using relatively small correlation windows (typically 32 × 32 pixels).

The correlation is a two steps process. The first step determines — at a multi-pixel scale — the shift between images from their correlation matrix. The second step refines the measurements at a sub-pixel scale by estimating the slope difference of the images' Fourier transform. To reduce windowing artifacts in the Fourier transforms, image patches are weighted with a Hanning window. Also, to improve further the correlation quality, a mask that filters out high frequencies is applied to the images' Fourier transforms.

Correlation is processed using a sliding window that scans the two images. Each correlation provides an offset in column and row directions, and a Signal to Noise Ratio (SNR, ranging from 0 to 1) which assess the measurement quality. In case of a UTM projection the measured offsets, in column and row, correspond directly to horizontal displacements along the East–West and North–South directions respectively.

3. Test results

3.1. The 1992, Mw 7.3, Landers earthquake

In Michel and Avouac (2006), the Kickapoo step over of the 1992 Landers, California, earthquake was studied successfully using USGS National Aerial Photography Program (NAPP) photographs (USGS, 1987). This program acquires images of the continental United States in a 5–7 year cycle. The aircraft altitude is around 20,000 feet (6100 m) and films are 9 × 9 in., covering an area of slightly less than 10 × 10 km. The ground resolution is announced at 1 m while the film nominal resolution is about 10 μm corresponding to around 0.4 m on ground. Michel and Avouac (2002) used films scanned at 10 μm with a microdensitometer (MD) originally designed for astronomy with a theoretical positional accuracy of 0.6 μm and a root mean square error (rmse) of 0.2 μm. However, errors of up to 1 μm in repetitiveness were observed, leading to ground errors of up to 4 cm. In practice, access to a microdensitometer may be limited. To validate our methodology with more easily available data, we have studied the same case example using films scanned at 21 μm delivered by the USGS (Table 1).

Regarding the DEM, we used the freely available SRTM DEM, with a ground resolution of 1 arc-s (∼30 m). It has an absolute height accuracy of 16 m and a relative height accuracy of 10 m. The absolute horizontal accuracy is 20 m and the relative horizontal accuracy is 15 m. These accuracies are quoted at 90% level (JPL-NASA, 2000). The IO of the 1989 and 1995 images were established with the help of the camera calibration reports provided by the USGS. The 1995 image was co-registered first to the topography as the SRTM mission was carried out in 2000 (both post-earthquake). A shaded image of the DEM was generated (Fig. 1) with illumination parameters estimated from the 1995 image shadow pattern. Four GCPs were selected between the image and the shaded DEM. Horizontal and vertical coordinates were both obtained from the georeferenced DEM. Using patches of 256 × 256 pixels, GCPs were optimized according to the procedure outlined in 2.4. The average residual mis-registration was estimated to 2.4 m while the standard deviation residual was estimated to 18 m. This latter uncertainty is slightly higher than the 15 m relative horizontal accuracy of the SRTM DEM. More GCPs would have properly constrained the co-registration, but the limited topography in the image did not allow it. The 1995 EO was determined using the optimized GCPs. The image was then orthorectified on a 1 m resolution grid (UTM, North, Zone 11).

Five tie points, quite distant from each other, were taken on one side of the fault between the orthorectified 1995 image and the raw 1989 image (the fault was localized after a coarse pre-process with tie points selected at the four image corners). Horizontal coordinates were obtained from the 1995 orthorectified image, and elevation was read from the DEM to convert these tie points into GCPs. GCP optimization was carried out with 256 × 256 pixels patches. After three iterations the optimization converged. The average residual mis-registration was evaluated to 1 mm, and the standard deviation residual to 35 cm. The 1989 image was

Table 1
Data references. Scans were obtained from the USGS and from a microdensitometer (MD) originally designed for astronomy. CIR: Color Infra-Red.

Study case	Date	NAPP code	Film type	Scan origin	Res. (μm)
Landers	07/25/1989	1790-161	CIR	USGS	14, 21
				MD	10
	10/03/1995	6825-253	B/W	USGS	7, 14, 21
				MD	10
	06/01/2002	12498-144	CIR	USGS	14, 21
Hector Mine	07/25/1989	1790-210	CIR	USGS	21
	06/01/2002	12488-50	CIR	USGS	21

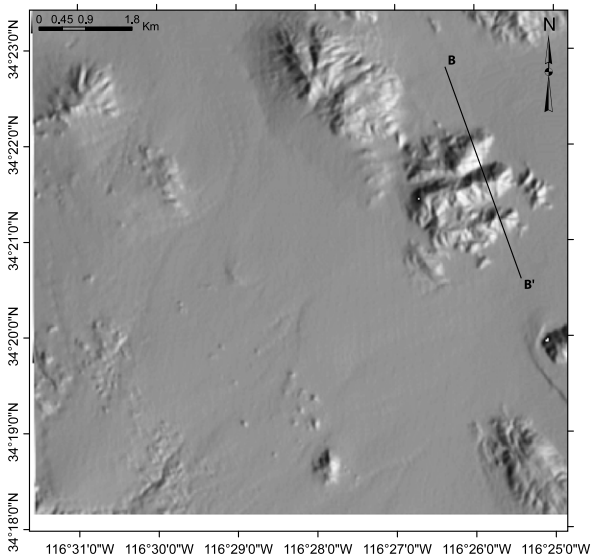

Fig. 1. Shaded DEM of the study area. Profile BB' locates the profile on Figs. 3 and 9, and reported on Fig. 10.

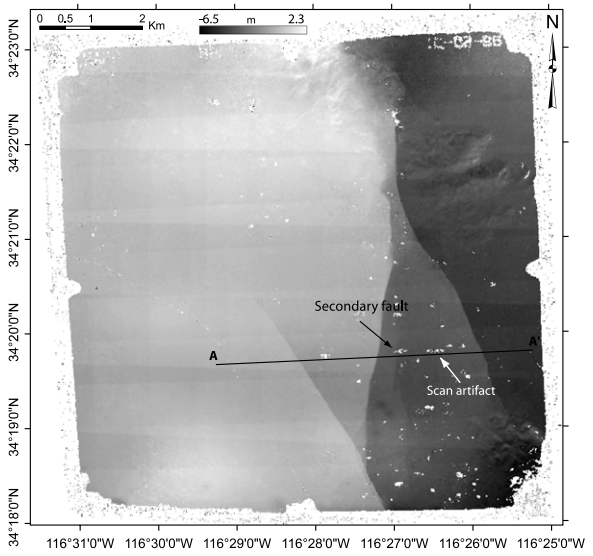

Fig. 2. North/South displacement map of the Landers 1989/1995 correlation. Images were orthorectified on a 1 m grid and correlated using a 64 × 64 pixel window with a 16 pixel step. Positive displacement is toward the North. The main fault shows up as the main discontinuities, as well as a secondary fault trace with a slip estimated at 20 cm. Film distortion and scan artifacts, with amplitude up to 40 cm, are visible. Profile AA' is reported on Fig. 5.

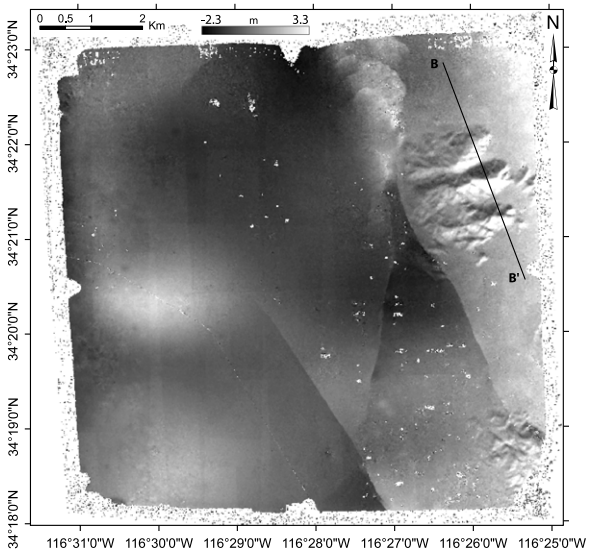

Fig. 3. East/West displacement map of the Landers 1989/1995 correlation. Images were orthorectified on a 1 m grid and correlated using a 64 × 64 pixel window with a 16 pixel step. Positive displacement is toward the East. Topography and film artifacts are visible on the right and left side of the map respectively. Topographic artifacts are due to a parallax effect caused by the use of a unique DEM for the 1989 and 1995 images although the earthquake changed the topography. Profile BB' is reported on Fig. 10.

orthorectified with the help of the optimized GCPs on the same 1995 orthorectified image grid.

Images were then correlated using a 64 × 64 pixel window (64 × 64 m on the ground), with a 16 pixel sliding step. The results of the correlation process are presented in Figs. 2–4. The fault ruptures appear clearly as discontinuities in the displacement maps. Horizontal fault slip is easily measured from profiles run perpendicular to the fault trace (Fig. 5). As also shown by Michel and Avouac (2006), the ruptures map and the measured fault slip are in excellent agreement with the field investigation of Sieh et al. (1993). To illustrate the potential of the technique we point to a secondary fault, mapped but not measured during field investigations, which is both detected and measured from the aerial photographs (Fig. 2). The horizontal slip is estimated to 20 cm (one-fifth of the images resolution) validating the sub-pixel change detection capability of the technique. In some areas, correlation is lost leading to very small SNR or outliers. Only 0.3% of the total number of measurements fall within this category. Inspection of the decorrelation areas show that they result from man made changes (new or modified buildings), or coincide with areas which are nearly translation invariant at the correlation window scale, e.g., radiometrically constant sandy areas, straight and isolated roads. It should be noted that the images were particularly suited to cross-correlation as NAPP follows strict acquisition specifications, e.g., no cloud cover, limited haze, and limited shading. A strong variation in sun illumination, for example, will cause shading and radiometric (depending on ground reflectance) differences in the images that can seriously compromise the correlation output.

To assess the potential bias and error of the measurements, an image of 2002 was co-registered to the 1995 orthorectified image with 13 GCPs. The GCP optimization, carried out with 256 × 256 pixel patches, converged after 4 iterations. The average residual mis-registration was evaluated to 2 mm and the standard deviation residual to 30 cm. Results of the correlation are presented in Figs. 6

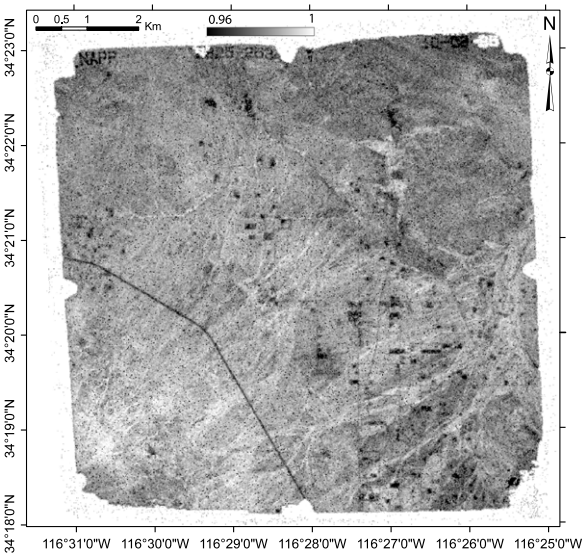

Fig. 4. SNR map of the Landers 1989/1995 correlation. A higher SNR indicates a better correlation. Roads are visible and get a low SNR due to the poor correlation algorithm convergence on translation invariant features (Leprince et al., 2007). Other areas of decorrelation include man made changes. The total amount of decorrelation accounts for 0.3% of the measures.

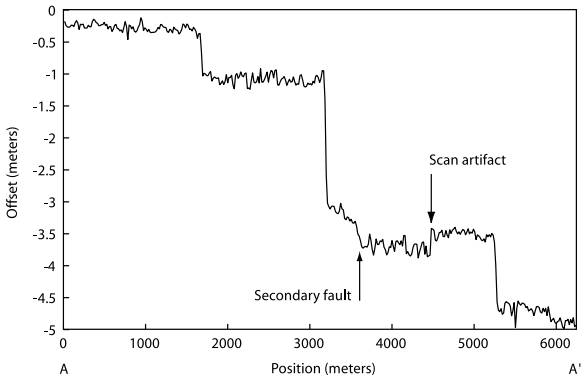

Fig. 5. Profile AA' from Fig. 2. Secondary fault with slip amplitude as low as 20 cm is detected and its location is indicated by a black arrow on Fig. 2. At around the same amplitude a scan artifact is also detected and is indicated by a white arrow on Fig. 2. The standard deviation of the measurements is 7 cm.

and 7. No significant ground deformation is expected given that the only large earthquake in the area over that period of time is the 1999, Mw 7.1, Hector Mine, California, earthquake which occurred about 30 km away from the study area. Locally, the measurement spread is Gaussian with a standard deviation of 7 cm. However, geometric artifacts mainly due to scan artifacts and film distortion cause the global measurement histogram to be not Gaussian with a spatially dependent distribution. The histogram is however centered at around zero, with a standard deviation of 25 cm and an amplitude maximum of up to 1 m.

As seen in the East/West displacement map (Fig. 7), deformation is everywhere negligible except along the 1992 fault trace event where some small amount of displacement are detected. This displacement corresponds to a right-lateral slip of about 10–15 cm. The possibility of a parallax effect due to a vertical up/down lift not accounted for in the DEM is discarded. Indeed, from Eq. (1), a 4 m up/down-lift would be necessary to cause a 15 cm horizontal parallax displacement. The displacement observed on the E–W component might be real and could correspond to aseismic slip triggered by the 1999, Hector Mine, earthquake, as reported on some other faults by Fialko et al. (2001) and discussed by Du et al. (2003). However, this deformation does not show up in the

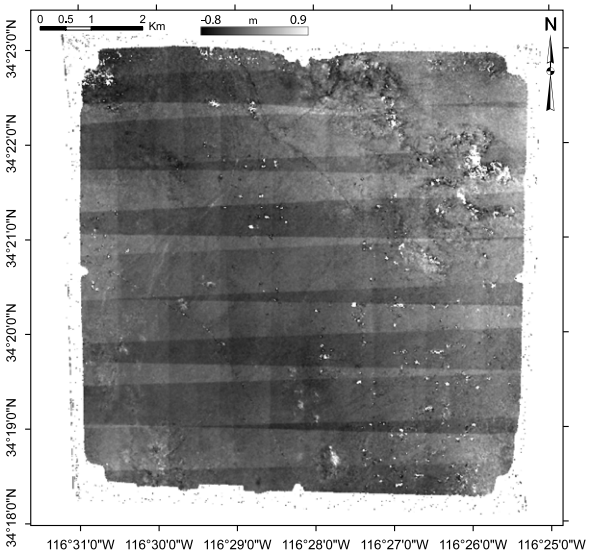

Fig. 6. North/South displacement map of the Landers 1995/2002 correlation. Images were orthorectified on a 1 m grid and correlated using a 64 × 64 pixel window with a 16 pixel step. Strong scan artifacts are visible along the line and column directions. They have an amplitude up to 40 cm, which is above the 20 cm fault detected in Fig. 2, and can limit the technique depending on their amplitude and location. Notice that the fault displacement detected in Fig. 7 does not appear here, although it may be masked by the strong scan artifacts.

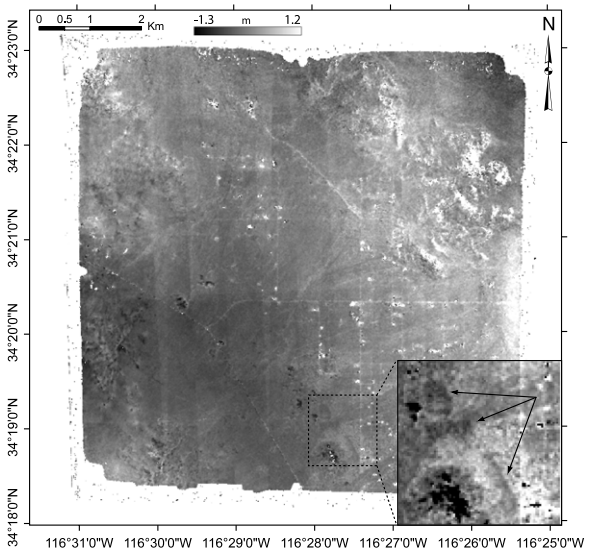

Fig. 7. East/West displacement map of the Landers 1995/2002 correlation. Images were orthorectified on a 1 m grid and correlated using a 64 × 64 pixel window with a 16 pixel step. Inspection of decorrelation areas on topography revealed non negligible shadowing differences. Slight scan artifacts are visible in the column direction. Black arrows indicates fault displacements with an amplitude estimated at around 10–15 cm. No clear explanation has yet been found. A parallax effect due to a vertical uplift not accounted for in the DEM is discarded as 4 m of up/down lift would be necessary.

North/South displacement map, possibly because it is obscured by the particularly strong scan artifacts on this component (Fig. 6).

3.2. Sensitivity to DEM artifacts

Topographic artifacts are seen on both 1989/1995 and 1995/2002 displacement maps, as suggested by the obvious correlation with the shaded topography (Figs. 1–3). The artifacts are most obvious on the 1989/1995 displacement map (Fig. 3) in the area of profile BB' where the relief is the roughest. A simple inter-

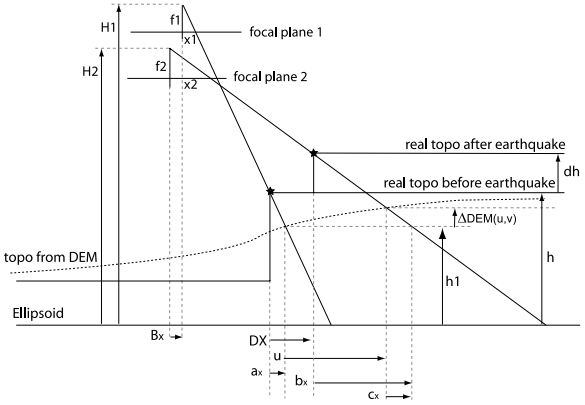

Fig. 8. Geometry of the orthorectification and correlation measure in case of a unique DEM use (in one dimension) when other possible artifacts are considered null (film distortions, correlator bias, …). DX and u represent the real and measured horizontal displacement in the *x* direction.

pretation of this correlation is that the change of the topography due to co-seismic deformation cannot be ignored.

Assuming a perfect acquisition system and ignoring film distortions, scan errors, and correlation bias, the effect of the change of the topography (Fig. 8) can be accounted for by writing:

$$\begin{cases} DX = \underbrace{(h-h_1)\dfrac{x_1}{f_1}}_{a_x} + u - \underbrace{(h-h_1+dh)\dfrac{x_2}{f_2}}_{b_x} + \underbrace{\Delta DEM(u,v)\dfrac{x_2}{f_2}}_{c_x} \\ DY = (h-h_1)\dfrac{y_1}{f_1} + v - (h-h_1+dh)\dfrac{y_2}{f_2} + \Delta DEM(u,v)\dfrac{y_2}{f_2} \end{cases} \quad (1)$$

where DX and u refer respectively to the real and measured displacements in the East/West direction. DY and v apply to the North/South direction. Subscripts 1 and 2 refer to the master and slave images. h, h_1, and dh represent respectively, the real elevation of a ground point, the DEM elevation read at the ground point, and the vertical displacement of the ground point caused by the earthquake. f_1 and f_2 are the focal lengths of the master and slave cameras respectively, and x_1, y_1 and x_2, y_2 are the camera coordinates of the ground point image in the master and slave images respectively.Rearranging Eq. (1) and using standard trigonometric equalities we obtain: Box I where H_1 and H_2 are the optical center altitudes of the master and slave cameras respectively, and B_x, B_y are the optical center base in East/West and North/South direction respectively. *i* represents the displacement induced by the DEM elevation error, taking into account the difference of the exposure stations' location. It is the absolute DEM error $(h - h_1)$ weighted by the stereoscopic parallax coefficient at the ground point considered. This coefficient is composed of an acquisition altitudes ratio, and the base/height ratio. *ii* represents the term originating from the approximation of the topography by a single DEM. The corresponding artifacts are thus correlated to the topographic gradients and can then be easily identified. *iii* represents the horizontal offset resulting from a vertical displacement not accounted for when using a single DEM.

Field investigations by Sieh et al. (1993) have shown that vertical displacement in the Kickapoo area was small everywhere compared to the horizontal displacements. *iii* can therefore be neglected. Moreover, from the EOs of the 1989 and 1995 images, optical centers are close enough that stereoscopic parallax effects are also negligible. Considering that the co-seismic displacements are at most a few meters, we then have $(B_x + DX) \ll H_1$. In addition, we have $H_1 \approx H_2$, so that *i* can be neglected. *i* is indeed estimated to at most 6 cm, assuming a DEM error of 16 m, in the upper range of estimated errors on the SRTM DEM. The real

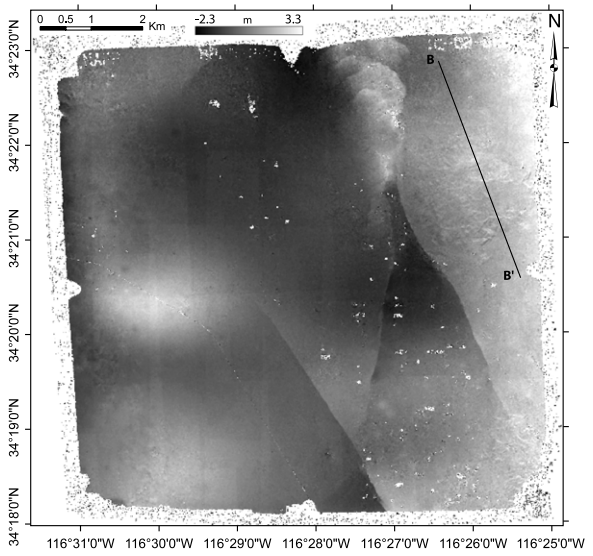

Fig. 9. East/West displacement map of the Landers 1989/1995 correlation corrected for artifacts due to a single DEM use, according to Eq. (1). Profile BB' is reported on Fig. 10.

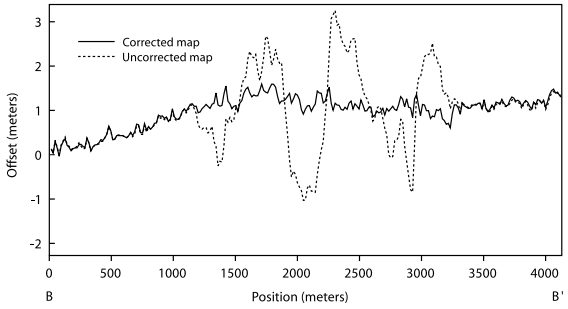

Fig. 10. Profile BB' of the uncorrected (Fig. 3) and corrected (Fig. 9) East/West displacement map. Notice that artifacts are correlated to the topography (Fig. 1).

displacements given by Box I are then estimated by correcting the displacements determined from the correlation maps according to:

$$\begin{cases} DX = \dfrac{x_2}{f_2}\Delta DEM(u,v) + u \\ DY = \dfrac{x_2}{f_2}\Delta DEM(u,v) + v \end{cases} . \quad (2)$$

Using the apparent displacements estimated from the correlation maps (u, v), the DEM, and the slave image information, the corrected displacement field (DX, DY) can thus be retrieved. This correction is very effective in our case study: the topographic artifacts are no longer visible in Figs. 9 and 10. This simple procedure allows the correction of the correlation map for the DEM artifacts induced by the use of a single DEM. Note that in the case of a significant vertical displacement, the term *iii* in Eq. (1) cannot be neglected. In that case the measured offsets (u, v) are a linear combination of the horizontal and vertical displacements (DX, DY, dH). All three components of the displacement can be determined only if a second pair of images with a different viewing angle is available.

3.3. Sensitivity to scan characteristics

3.3.1. Scan artifacts

In addition to topographic artifacts, scan artifacts are visible in both 1989/1995 and 1995/2002 displacement maps (Figs. 2, 3, 6 and 7) in the North/South and East/West directions. The artifacts

$$\begin{cases} DX = \underbrace{(h-h_1)\left[\frac{x_2}{f_2}\left(\frac{H_2-h-dh}{H_1-h}-1\right)-\frac{B_x+DX}{H_1-h}\right]}_{i} + \underbrace{\frac{x_2}{f_2}\Delta DEM(u,v)}_{ii} - \underbrace{\frac{x_2}{f_2}dh}_{iii} + u \\ DY = (h-h_1)\left[\frac{y_2}{f_2}\left(\frac{H_2-h-dh}{H_1-h}-1\right)-\frac{B_y+DY}{H_1-h}\right] + \frac{y_2}{f_2}\Delta DEM(u,v) - \frac{y_2}{f_2}dh + v \end{cases}$$

Box I.

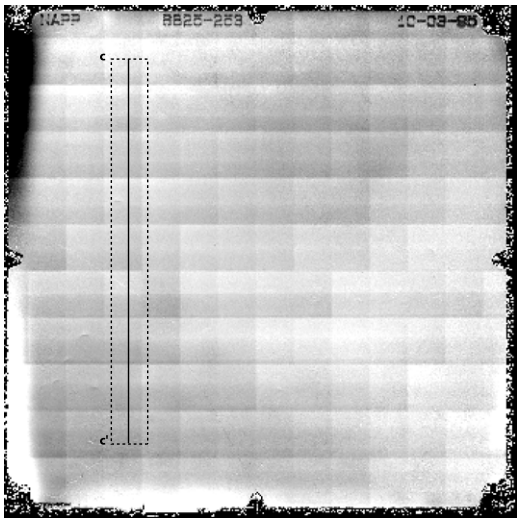

Fig. 11. Displacement map along the line direction of the MD/USGS scans correlation. Scans of the 1995 film were obtained at 21 μm from the USGS and at 10 μm from a MD. MD scan was co-registered and wrapped onto the USGS scan using a sinc kernel for resampling. Correlation used a 64 × 64 pixel window with a 32 pixel step. Scan artifacts are also visible in the column direction but with smaller amplitude. Profile CC' is reported on Fig. 12. Other long wavelength deformation are due to film distortions and mis-registration.

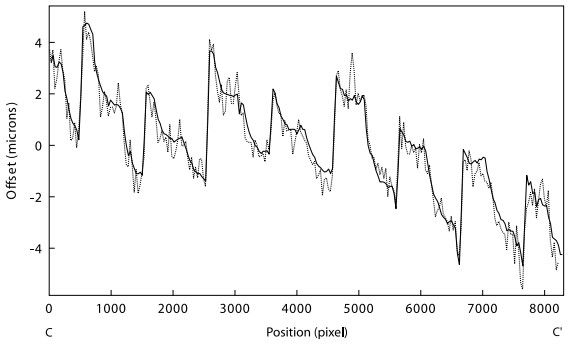

Fig. 12. Profile CC' (Fig. 11) showing scan artifacts with amplitude up to 5 μm (around 20 cm on ground), above the scanner specifications announced at 1.5 μm rmse.

Table 2
USGS scan artifacts amplitude measured in row and column direction. Scans from the USGS are wrapped onto scans from an MD and correlated using a 64 × 64 pixel sliding window.

Year	Master scan MD (μm)	Slave scan USGS (μm)	Max artifacts row (μm)	Max artifacts column (μm)
1989	10	14	20	10
	10	21	8	4
1995	10	7	6	4
	10	14	6	4
	10	21	5	3

amplitude in the North/South (line) direction is the largest and accounts for up to 40 cm on the ground.

To assess the quality of USGS digitized images, additional 1989 and 1995 film scans at 7 and 14 μm were obtained from the USGS (Table 1). A Zeiss Precision Scanner using a PHODIS Photogrammetric Image Processing System and a Leica Geosystems DSW600 Digital Scanning Workstation were used for the digitization. Both instruments are attributed a positional accuracy of 1.5 μm (rmse) (USGS personal communication).

These scans were compared to the MD scans of Michel and Avouac (2006) as the MD offers a practical positional accuracy of 1 μm (rmse). 1989 and 1995 USGS images were co-registered using manual tie points selection, wrapped (simple affine transformation), and correlated to the 1989 and 1995 MD images respectively. Note that, in this particular test, the images were not orthorectified, they were left in the camera geometry to avoid introducing other geometric artifacts. Apart from some long wavelength artifacts due to imprecision in co-registration and film distortions, scan artifact patterns are easily recognizable (Figs. 11 and 12). The artifacts amplitude are presented in Table 2. Artifacts measured along the line and column directions are clearly visible, with larger amplitude found in the line direction. Scans at 7 and 14 μm provided different patterns but no better stability than scans at 21 μm. The artifacts are smaller on the B/W scans than on the color-infrared (CIR) scans. Surprisingly, the 21 μm B/W scans present the smallest artifacts.

The observed scan artifacts, which are much stronger than what the nominal characteristic of the scanners would suggest, may put a severe limitation on the technique depending on their amplitude and orientation relative to the displacement to measure. However, scan artifacts produce patterns that are easily identified and relevant information (e.g. surface rupure map and fault slip) might be retrieved correctly from the correlation map using adequate care (Fig. 5).

3.3.2. Scan resolution

The photographs of the USGS NAPP program have an estimated ground resolution of 1 m, although the film's nominal resolution is around 40 cm. Scans at 7, 10, 14, and 21 μm correspond to an average ground resolution of 20, 40, 56, and 84 cm respectively. Displacement maps obtained from scans at 7, 10, 14 and 21 μm did not present any improvement with increasing scan resolution. The quality of the measurement even degrades with the scan resolution due to the stronger scan artifacts as discussed above. For this particular study, a scan resolution close to the nominal image resolution is sufficient; higher scan resolution do not deliver additional information.

3.4. Sensitivity to GCPs

3.4.1. GCPs — absolute accuracy

To assess the sensitivity of the technique to the choice and accuracy of GCPs, the 1995 aerial photograph was orthorectified with 4 different GCP sets:

- case 1–10 GCPs obtained from a field survey using a differential Real Time Kinematics GPS, with an accuracy of a few centimeters.

- case 2–10 GCPs optimized with a 10 m ground resolution orthorectified SPOT image (which georeferencing was optimized with the shaded SRTM DEM).
- case 3–4 GCPs optimized with the shaded SRTM DEM.
- case 4–4 GCPs carefully selected manually but not optimized from the shaded SRTM DEM. This case simulates the situation where a poorly contrasted shaded DEM due to low relief prevents a good correlation during the optimization.

Orthorectified images from cases 2, 3, and 4 were correlated with the image from case 1, considered as the reference. The displacement maps show long wavelength distortions with some high frequency distortions correlated to the topography. Maximal mis-registrations are 10 m, 18 m, and 25 m for case 1/2, case 1/3, and case 1/4, respectively. Case 2 and case 3 are within the SRTM DEM absolute horizontal accuracy (20 m), whereas case 4 is outside. Although the SPOT image was also coregistered with the shaded SRTM DEM, case 2 absolute georeferencing is better than case 3. This is explained by the larger area and larger number of GCPs (∼20) used to coregister the SPOT image to the shaded DEM.

To assess the consequence of these mis-registrations on the co-seismic displacement maps, the 1989 slave image was co-registered and correlated with the four-case 1995 orthorectified images. The results were found to be similar regarding the surface rupture mapping and fault slip vectors. However, long wavelength displacements were different.

3.4.2. GCPs — Tectonic signal distortions

The major source of distortion at long wavelength found in 3.4.1 comes from the assumption made during the slave image's GCP definitions. Indeed, tie points are selected between the slave and the orthorectified master to co-register the two images. These tie points are converted to GCPs using the orthorectified master georeferencing for horizontal coordinates and the DEM for the vertical coordinate (elevation). The possible ground displacement at each GCP location is then cancelled out by equating the slave ground coordinates with the master ground coordinates for each GCP. We illustrate this from NAPP aerial images of the 1999, Mw 7.1, Hector Mine, California, earthquake (Table 1). Pre- and post- earthquake images were processed using the methodology described in 2. Three tie points were selected between the slave and orthorectified master and the derived GCPs were optimized. The North/South displacement map is presented in Fig. 13. The 2D displacement is overlaid as vectors on the figure, together with the GCP locations. The fault rupture is clearly visible. Its geometry and horizontal slip are in accordance with the field measurements by Treiman et al. (2002). As expected, displacement falls to zero at GCP locations. The co-registration compensated the real ground displacements at the GCP locations and introduced long wavelength distortion in the displacement maps. Forcing the co-registration at GCP locations without accounting for the ground displacement introduces long wavelength distortion biasing ground displacements in the far-field.

This bias can be avoided if estimates of the ground displacements at the GCP locations are known and taken into account during the optimization. To demonstrate this point we used the Hector Mine earthquake displacement maps determined from the correlation of 10 m SPOT images (Leprince et al., 2007). The SPOT images were co-registered using GCPs far away from the fault zone where co-seismic displacement could be neglected. A subset of the North/South displacement map obtained from the SPOT images is shown in Fig. 14. The dashed square represents the aerial images footprint.

The GCPs of the aerial slave image were then re-optimized taking into account the displacements measured from SPOT at the three GCP locations (Fig. 14). The North/South component of the

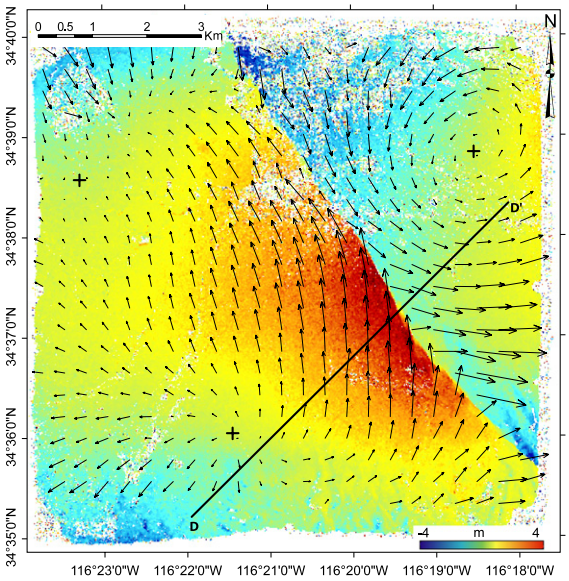

Fig. 13. North/South displacement map of the 1989/2002 correlation of images bracketing the Hector Mine earthquake. Images were orthorectified on a 1 m grid and correlated using a 64 × 64 pixel window with a 16 pixel step. Three GCPs, indicated by the black crosses, were optimized to co-register the master and slave images without accounting for seismic ground displacement at their ground location. Overprinted vectors were generated from the North/South and East/West displacement maps, and represent the 2D ground displacement. Long wavelength distortions (vortices) are introduced to satisfy the master and slave co-registration. Profile DD' is reported on Fig. 16.

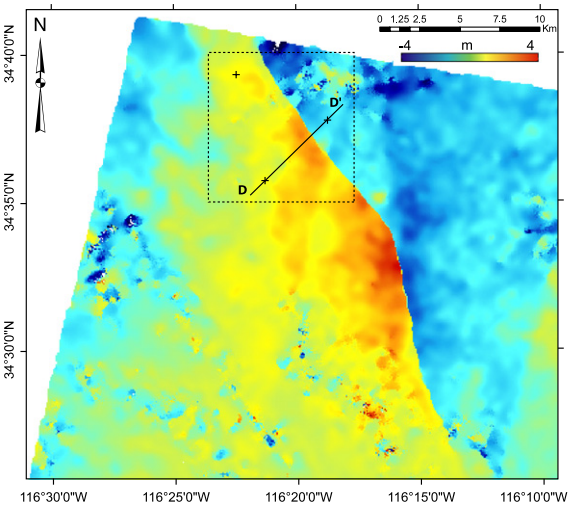

Fig. 14. North/South displacement map of the denoised SPOT correlation of images bracketing the Hector Mine earthquake. Three GCPs located far enough away from the fault to assume a null ground displacement were optimized to co-register the master and the slave. Images were orthorectified on a 10 m resolution grid and correlated using a 32 × 32 pixel window with an 8 pixel step. Positive displacement is toward the North. The raw displacement maps were denoised by a technique preserving fault offset (personal communication, Leprince). The dotted square represents the aerial photograph footprint, and black crosses indicate the location of the aerial photograph GCPs. Profile DD' is reported on Fig. 16.

displacement obtained from this procedure is shown in Fig. 15. The fault geometry and fault slip value are identical to the ones from the first process. However, the long wavelength component of the displacement map now matches the SPOT displacement map, and the distortion found on Fig. 13 was corrected. Nevertheless, far-field ground deformation must be considered carefully with film based imagery as film distortion, for example, manifests itself in the displacement map by deformation of similar frequency and amplitude (e.g., Fig. 3).

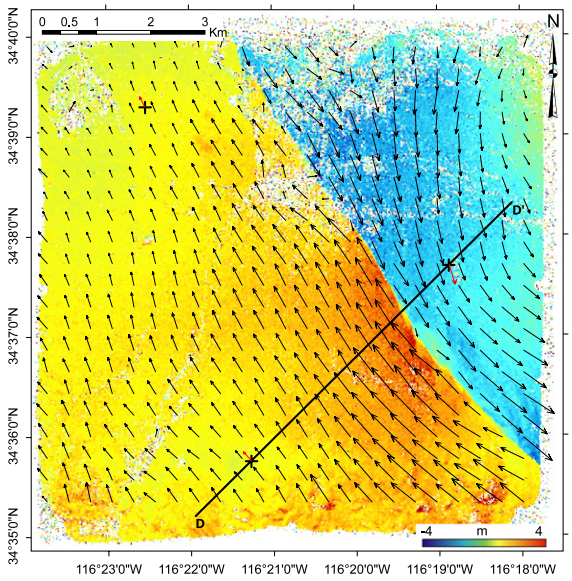

Fig. 15. North/South displacement map of the 1989/2002 correlation map of images bracketing the Hector Mine earthquake. Images were orthorectified on a 1 m grid and correlated using a 64 × 64 pixel window with a 16 pixel step. Three GCPs, located by the black crosses, were optimized to co-register the master and the slave images while accounting for ground displacement at their ground location (red arrow) from SPOT measures (Fig. 14). Major long wavelength distortions seen in Fig. 13 were removed. Only the long wavelength distortions caused by the SPOT correlation error may remain, along with those introduced by film distortions. Profile DD' is reported on Fig. 16.(For interpretation of the references to colour in this figure legend, the reader is referred to the web version of this article.)

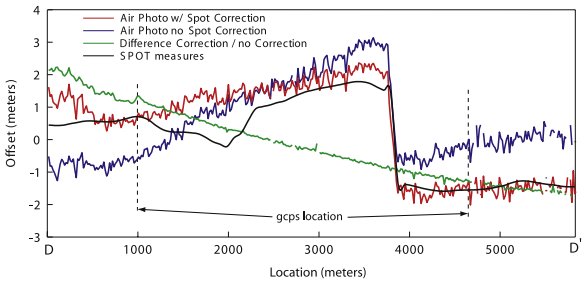

Fig. 16. Profiles from Figs. 13–15. GCP correction brings a 2nd order polynomial correction in each North/South and East/west direction. High frequency signals such as the fault slip, are not affected however.

4. Conclusion

This study describes how the procedure originally developed to process optical satellite images can be adapted to aerial photographs, taking into account the specific characteristics of these types of images. Orthorectification and georeferencing can be achieved using the DEM only, without any other external data. In that case, the absolute georeferencing of the images is limited by the accuracy of the DEM georeferencing. The correlation of two images taken before and after an earthquake yields offsets which primarily represent the ground horizontal displacements. Some artifacts are introduced when using a single DEM, but they can be corrected in postprocessing. In case of large stereoscopic parallax and significant ground up/down lift, the horizontal displacements measured also depend on the vertical displacement; however, Box I, Eq. (2) suggest that horizontal and vertical displacement can be retrieved if a third image is available, or, alternatively, if a pair of images from the adjacent flight strip overlaps the area of interest. The images co-registration is achieved with a sub-pixel accuracy of around 1/3 of a pixel. The limitation on the images' co-registration comes from film distortions, scan artifacts, DEM error, and the assumption of no ground displacements at the tie point locations. This latter assumption can be reduced if the ground displacements at the tie point locations can be estimated independently (from other measurements or an a priori model of co-seismic ground deformation). Better performance should be achievable in the future thanks to the rapid spread of digital aerial photography and to a better control on the geometry of the images thanks to Real-Time-Kinematic GPS and Inertial Navigation Unit. Finally, the technique is sensitive to temporal decorrelation such as those due to shadowing differences, man made changes, changes of the vegetation cover and clouds.

Despite these limitations, this study presented a powerful technique to precisely map the fault trace and measure fault slip and near-field ground deformation. With images at 1 m resolution, the technique applies to ruptures with a minimum length of a few kilometers and a minimum displacement of a few tens of centimeters. It should thus be applicable to earthquakes breaking the surface with a moment magnitude exceeding about 6.5. This opens the possibility to reassess a number of past earthquakes for which aerial photography archives would be available. Aerial photographs are less adapted to measuring ground deformation in the far-field which will be best measured with optical satellite imagery (e.g. SPOT, ASTER) or interferometric synthetic aperture radar. Aerial photographs and these latter techniques are complementary as they provide unprecedented accuracy in the near- and far-field measurements, respectively.

Seismotectonic applications have been the primary motivation for this study, but the method described here is also applicable to measure ice flow, landslides or sand dune migration for example (Leprince et al., 2008). The algorithms were implemented in the software package COSI-Corr (ENVI module) complementing the satellite image processing package. The software is available from the Tectonics Observatory (http://www.tectonics.caltech.edu/).

Acknowledgements

The authors would like to thank R. Michel and R. Binet (Laboratoire de Detection Geophysique, CEA, France) for their insightful comments and the valuable discussions on their early work; the anonymous reviewers whose comments have helped clarified a number of points; and Lionel Keene (Caltech) for the proofreading. This work was partly funded by NSF grant EAR 0636097 and by the Gordon and Betty Moore Fundation. This is Tectonic Observatory contribution 92.

References

Avouac, J.-P., Ayoub, F., Leprince, S., Konca, O., Helmberger, D.V., 2006. The 2005, M-w 7.6 Kashmir earthquake: Sub-pixel correlation of ASTER images and seismic waveforms analysis. Earth and Planetary Science Letters 249 (3–4), 514–528.

Binet, R., Bollinger, L., 2005. Horizontal coseismic deformation of the 2003 Bam (Iran) earthquake measured from SPOT-5 THR satellite imagery. Geophysical Research Letters 32 (2), L02307.

de Michele, M., Briole, P., 2007. Deformation between 1989 and 1997 at Piton de la Fournaise volcano retrieved from correlation of panchromatic airborne images. Geophysical Journal International 196 (1), 357–364.

Delacourt, C., Allemand, P., Casson, B., Vadon, H., 2004. Velocity field of the "La Clapiere" landslide measured by the correlation of aerial and QuickBird satellite images. Geophysical Research Letters 31 (15), L15619.

Dominguez, S., Avouac, J., Michel, R., 2003. Horizontal coseismic deformation of the 1999 Chi-Chi earthquake measured from SPOT satellite images: Implications for the seismic cycle along the western foothills of central Taiwan. Journal of Geophysical Research - Solid Earth 108 (B2), 2083.

Du, W., Sykes, L., Shaw, B., Scholz, C., 2003. Triggered aseismic fault slip from nearby earthquakes, static or dynamic effect? Journal of Geophysical Research - Solid Earth 108 (B2), 2131.

Feigl, K., Sarti, F., Vadon, H., McClusky, S., Ergintav, S., Durand, P., Burgmann, R., Rigo, A., Massonnet, D., Reilinger, R., 2002. Estimating slip distribution for the Izmit mainshock from coseismic GPS, ERS-1, RADARSAT, and SPOT measurements. Bulletin of the Seismological Society of America 92 (1), 138–160.

Fialko, Y., Simons, M., Agnew, D., 2001. The complete (3-D) surface displacement field in the epicentral area of the 1999 M(w)7.1 Hector Mine earthquake, California, from space geodetic observations. Geophysical Research Letters 28 (16), 3063–3066.

Hudnut, K.W., Bock, Y., Cline, M., Fang, P., Feng, Y., Freymueller, J., Ge, X., Gross, W.K., Jackson, D., Kim, M., King, N.E., Langbein, J., Larsen, S.C., Lisowski, M., Shen, Z.-K., Svarc, J., Zhang, J., 1994. Co-seismic displacements of the 1992 landers earthquake sequence. Bulletin of the Seismological Society of America 84 (3), 625–645.

JPL-NASA, 2000. Shuttle Radar Topography Mission. http://www2.jpl.nasa.gov/srtm/statistics.html (accessed April 1, 2009).

Klinger, Y., Xu, X., Tapponnier, P., Van der Woerd, J., Lasserre, C., King, G., 2005. High-resolution satellite imagery mapping of the surface rupture and slip distribution of the M-W similar to 7.8, 14 November 2001 Kokoxili Earthquake, Kunlun Fault, northern Tibet, China. Bulletin of the Seismological Society of America 95 (5), 1970–1987.

Leprince, S., Barbot, S., Ayoub, F., Avouac, J.-P., 2007. Automatic and precise orthorectification, coregistration, and subpixel correlation of satellite images, application to ground deformation measurements. IEEE Transactions on Geoscience and Remote Sensing 45 (6, Part 1), 1529–1558.

Leprince, S., Berthier, E., Ayoub, F., Delacourt, C., Avouac, J., 2008. Monitoring earth surface dynamics with optical imagery. Eos, Transactions, AGU 89 (1), 1–2.

Michel, R., Avouac, J., 2002. Deformation due to the 17 August 1999 Izmit, Turkey, earthquake measured from SPOT images. Journal of Geophysical Research - Solid Earth 107 (B4), 2062.

Michel, R., Avouac, J., 2006. Coseismic surface deformation from air photos: The Kickapoo step over in the 1992 Landers rupture. Journal of Geophysical Research - Solid Earth 111 (B3), B03408.

Schwarz, K., Chapman, M., Cannon, M., Gong, P., 1993. An integrated INS/GPS approach to the georeferencing of remotely sensed data. Photogrammetric Engineering & Remote Sensing 59 (11), 1667–1674.

Sieh, K., Jones, L., Hauksson, E., Hudnut, K., Eberhart-Phillips, D., Heaton, T., Hough, S., Hutton, K., Kanamori, H., Lilje, A., Lindvall, S., McGill, S., Mori, J., Rubin, C., Spotila, J., Stock, J., Kie Thio, H., Treiman, J., Wernicke, B., Zachariasen, J., 1993. Near-field investigations of the Landers earthquake sequence, April to July 1992. Science 260 (5105), 171–176.

Treiman, J., Kendrick, K., Bryant, W., Rockwell, T., McGill, S., 2002. Primary surface rupture associated with the M-w 7.1 16 October 1999 Hector Mine earthquake, San Bernardino County, California. Bulletin of the Seismological Society of America 92 (4), 1171–1191.

USGS, 1987. National Aerial Photography Program (NAPP). http://edc.usgs.gov/guides/napp.html (accessed April 1, 2009).

Van Puymbroeck, N., Michel, R., Binet, R., Avouac, J., Taboury, J., 2000. Measuring earthquakes from optical satellite images. Applied Optics 39 (20), 3486–3494.

Wolf, P., Dewitt, B., 2000. Elements of Photogrammetry with Applications in GIS, 3rd ed. Mc Graw Hill.